



SUBJECT AREAS:
BIOPHOTONICS
SPECTROSCOPY
BIOPHYSICS
BIOMEDICAL ENGINEERING

Received
11 December 2012
Accepted
14 February 2013
Published
28 February 2013

Correspondence and
requests for materials
should be addressed to
G.Y. (guoqiang.yu@
uky.edu)

* These authors
contributed equally to
this work.

Simultaneous measurement of deep tissue blood flow and oxygenation using noncontact diffuse correlation spectroscopy flow-oximeter

Ting Li^{1*}, Yu Lin^{1*}, Yu Shang¹, Lian He¹, Chong Huang¹, Margaret Szabunio² & Guoqiang Yu¹

¹Center for Biomedical Engineering, University of Kentucky, Lexington, KY 40506-0070, USA, ²Markey Cancer Center, University of Kentucky, Lexington, KY 40536-0093, USA.

We report a novel noncontact diffuse correlation spectroscopy flow-oximeter for simultaneous quantification of relative changes in tissue blood flow (*rBF*) and oxygenation ($\Delta[\text{oxygenation}]$). The noncontact probe was compared against a contact probe in tissue-like phantoms and forearm muscles ($n = 10$), and the dynamic trends in both *rBF* and $\Delta[\text{oxygenation}]$ were found to be highly correlated. However, the magnitudes of $\Delta[\text{oxygenation}]$ measured by the two probes were significantly different. Monte Carlo simulations and phantom experiments revealed that the arm curvature resulted in a significant underestimation ($\sim -20\%$) for the noncontact measurements in $\Delta[\text{oxygenation}]$, but not in *rBF*. Other factors that may cause the residual discrepancies between the contact and noncontact measurements were discussed, and further comparisons with other established technologies are needed to identify/quantify these factors. Our research paves the way for noncontact and simultaneous monitoring of blood flow and oxygenation in soft and vulnerable tissues without distorting tissue hemodynamics.

Characterization of tissue blood flow, blood oxygenation and oxidative metabolism is important for the diagnosis and therapeutic assessment of vascular/cellular diseases^{1–7}. A wide range of imaging technologies have been developed to measure deep tissue hemodynamics/metabolism, including positron emission tomography (PET), magnetic resonance imaging (MRI), single photon emission computed tomography (SPECT), and Xenon computed tomography (Xenon CT). However, these techniques have some limitations impeding their routine use in clinics, such as large instrumentation, high cost and poor mobility^{8,9}. Some of them also involve exposure to ionizing radiation (e.g., PET, SPECT, Xenon CT).

Near-infrared spectroscopy (NIRS) was initiated in 1977 by Jöbsis¹⁰ as a simple, fast, portable, relatively inexpensive method for noninvasive quantification of deep tissue oxygenation^{11,12}. Traditional NIRS takes advantage of the low absorption spectrum of tissue in the near-infrared (NIR) range (650–950 nm) and penetrates deep tissue (up to several centimeters¹³) to detect light absorption by chromophores such as oxy- and deoxy-hemoglobin (HbO_2 and Hb). An emerging dynamic NIR technology, diffuse correlation spectroscopy (DCS), has been developed to measure the relative change of blood flow (*rBF*) in deep microvasculature^{14–20}. DCS uses coherent NIR light to monitor temporal light intensity fluctuations caused by moving scatterers (primarily red blood cells (RBCs) in tissues) for extracting blood flow index (*BFI*) and *rBF*. DCS has also been combined with NIRS in hybrid instruments and simple models have been used to estimate tissue oxygen metabolism from the measured blood flow and oxygenation data^{16,17,19,21,22}. The hybrid NIRS/DCS instruments, while effective, are relatively large, complex and expensive.

Our group has recently developed and validated a truly portable and relatively inexpensive dual-wavelength DCS flow-oximeter for simultaneous measurement of *rBF* and relative changes in oxy- and deoxy-hemoglobin concentrations (i.e., $\Delta[HbO_2]$ and $\Delta[Hb]$)²³. Instead of physically combining the NIRS and DCS, which increases the instrument cost and dimensions, the dual-wavelength DCS flow-oximeter extracts $\Delta[HbO_2]$ and $\Delta[Hb]$ via recording light intensity changes at two wavelengths (785 and 853 nm). The only adaptation necessary to achieve this function is the addition of a second laser diode to the single-wavelength DCS flow device. Being truly portable, easy-to-use and inexpensive, the DCS flow-oximeter is ideal for bedside monitoring in clinics^{23–29}.



Most previous NIR studies have measured tissue hemodynamics/metabolism using optical probes in contact with tissue surfaces^{11,12,19,21–23,26,28,30–32}. Significant problems with these contact measurements include increased risk of infection of ulcerous tissues and deformation of vulnerable/soft tissues (e.g., breast, muscle) resulted from probe-tissue contact. Deformation of vulnerable/soft tissues may distort measured tissue properties^{33–35}. It is nearly impossible to consistently apply the appropriate amount of pressure and achieve even coverage on vulnerable/soft tissues. In addition, the contact probe is uncomfortable for subjects. Only a few DCS studies have reported noncontact probing of tissue hemodynamics in small animals using camera probes with limited light penetration depth (< 0.5 cm)^{16,20}. Very recently, our group designed a noncontact DCS flow probe using two separate optical paths (instead of the single optical path used in the camera probes) for the source and detector³⁶. This unique design prevents interference between the source and detector paths and allows large separations between the source and detector (e.g., > 1 cm) for blood flow measurements in deep tissues³⁶.

The challenge remains for noncontact measurements of both blood flow and blood oxygenation in deep tissues. This study was designed to evaluate a noncontact dual-wavelength DCS flow-oximeter for simultaneous quantification of blood flow and oxygenation changes in deep tissues (e.g., human skeletal muscles). The noncontact DCS flow-oximeter probe was compared against a contact probe used previously^{20,37} in both tissue-like phantoms and human forearm muscles. The two probes were connected to two DCS flow-oximeter devices that acquired both flow and absorption/oxygenation data in phantoms/forearms. An ink-titration experiment was conducted to create the absorption change in tissue-like phantoms, and an arterial cuff-occlusion paradigm was applied on the upper arm to induce flow and oxygenation changes in forearm flexor muscles. Highly consistent trends in both flow and oxygenation changes were observed from the forearm muscles measured concurrently by the contact and noncontact probes. Surprisingly, the magnitudes of blood oxygenation changes measured by the noncontact probe were significantly smaller than those measured by the contact probe. Monte Carlo simulations and tissue-like phantom experiments revealed that the arm curvature resulted in a significant underestimation of the noncontact measurements in blood oxygenation but not in *rBF*. A calibration algorithm based on Monte Carlo simulations was then proposed to correct such underestimation. To the best of our knowledge, we present in this paper the *first* successful noncontact measurements of both blood flow and blood oxygenation in deep tissues using the noninvasive DCS flow-oximeter.

Results

Subject characteristics. Table 1 lists the forearm dimensions (d_1 and d_2), adipose tissue thickness (*ATT*), and baseline values of μ_a and μ_s' at the two wavelengths (measured by the Imagent tissue-oximeter) from the 10 subjects. These quantities were used to calculate *rBF*, DPF_λ and $\Delta[\text{oxygenation}]$ (see Methods section).

Tissue-like phantom experimental results. Figure 2 shows $\Delta\mu_a$ and flow index (D_B) changes during ink titrations ($\Delta\mu_a = 0.0125 \text{ cm}^{-1}$ at 785 nm for each step) measured by the noncontact and contact DCS flow-oximeter probes. The $\Delta\mu_a$ values measured by both probes agreed well with the theoretical values at both wavelengths (maximum discrepancies < 10%; Fig. 2a and Fig. 2c). The noncontact measurements of $\Delta\mu_a$ were highly correlated with the contact measurements at both wavelengths and the regression slopes were close to 1 (slope = 0.97, $R^2 = 0.99$, $p < 10^{-5}$ at 785 nm; slope = 0.94, $R^2 = 0.99$, $p < 10^{-5}$ at 853 nm; Fig. 2b and Fig. 2d). As expected, since adding ink did not change the Brownian motions (D_B) of Intralipid particles, flow values measured by both probes were fairly constant (maximum variations < 8%) and the discrepancy between the two measurements was < 5% throughout the titration steps (Fig. 2e). Taken together, the results from the phantom experiments indicated the high consistency of noncontact and contact measurements of flow index (D_B) and optical property ($\Delta\mu_a$) in a homogenous medium with semi-infinite geometry.

Cuff occlusion responses. Figure 3 shows typical responses of *rBF* (a) as well as $\Delta[\text{HbO}_2]$ and $\Delta[\text{Hb}]$ (c) during arterial cuff occlusion measured by the contact and noncontact probes in the forearm muscle of one subject. The dynamic trends and magnitudes in *rBF* responses measured by the two probes were similar (regression slope = 0.94, $R^2 = 0.94$, $p < 10^{-5}$; Fig. 3b). The dynamic trends in $\Delta[\text{HbO}_2]$ and $\Delta[\text{Hb}]$ were also similar (Fig. 3c), however, the magnitude of $\Delta[\text{oxygenation}]$ measured by the noncontact probe was significantly lower than that measured by the contact probe (regression slope = 0.40, $R^2 = 0.65$, $p < 10^{-5}$; Fig. 3d).

Similar response trends in both *rBF* ($R^2 = 0.83 \pm 0.09$, $p < 10^{-5}$; Fig. 4a) and $\Delta[\text{oxygenation}]$ ($R^2 = 0.76 \pm 0.16$, $p < 10^{-5}$; Fig. 4b) were observed from all subjects ($n = 10$). The magnitudes of *rBF* measured by the noncontact probe agreed well with those measured by the contact probe; the mean value of regression slopes (0.86 ± 0.20 ; Fig. 4a) was not significantly different from 1 ($p = 0.051$). By contrast, the magnitudes of $\Delta[\text{oxygenation}]$ measured by the two probes were significantly different; the mean value of regression slopes was much less than 1 (0.44 ± 0.12 , $p < 10^{-5}$; Fig. 4b).

Interestingly, the regression slopes of $\Delta[\text{oxygenation}]$ from the ten subjects (Fig. 4b) were found to be significantly correlated with the dimensions of the measured forearms: d_1 ($R^2 = 0.45$, $p = 0.03$; Fig. 5a) and d_2 ($R^2 = 0.46$, $p = 0.03$; Fig. 5b). By contrast, there were no correlations between the slopes of *rBF* and the dimensions of the measured forearms. These discoveries implied that the forearm curvature was one of the factors influencing blood oxygenation measurements.

Monte Carlo (MC) simulation results. To evaluate the curvature influence on noncontact measurements we carried out MC simulations. The forearm muscle was assumed to be homogeneous tissue with a curved surface on an elliptic cylinder, and the sources and detector were projected on that surface (Fig. 1c). Based on the measured mean values of tissue optical properties and forearm dimensions in our subjects (Table 1), we assigned homogenous

Table 1 | Subject characteristics

Subject #	1	2	3	4	5	6	7	8	9	10	mean \pm s. d.
d_1 (cm)	5.45	6.30	5.00	5.25	6.30	7.20	5.30	6.80	6.90	7.10	6.16 ± 0.84
d_2 (cm)	7.15	8.50	6.80	6.80	7.85	10.15	6.85	9.30	9.60	9.30	8.23 ± 1.30
<i>ATT</i> (cm)	0.35	0.37	0.26	0.42	0.38	0.42	0.33	0.48	0.38	0.30	0.37 ± 0.06
μ_a (cm^{-1} , 785 nm)	0.20	0.15	0.12	0.12	0.17	0.15	0.15	0.15	0.18	0.08	0.15 ± 0.03
μ_s' (cm^{-1} , 785 nm)	4.29	5.42	7.99	7.33	7.61	5.40	7.87	8.48	7.76	4.98	6.71 ± 1.51
μ_a (cm^{-1} , 853 nm)	0.21	0.18	0.15	0.13	0.18	0.17	0.16	0.17	0.20	0.11	0.17 ± 0.03
μ_s' (cm^{-1} , 853 nm)	3.88	5.00	7.67	6.99	6.71	5.08	7.01	7.80	6.75	5.74	6.26 ± 1.20

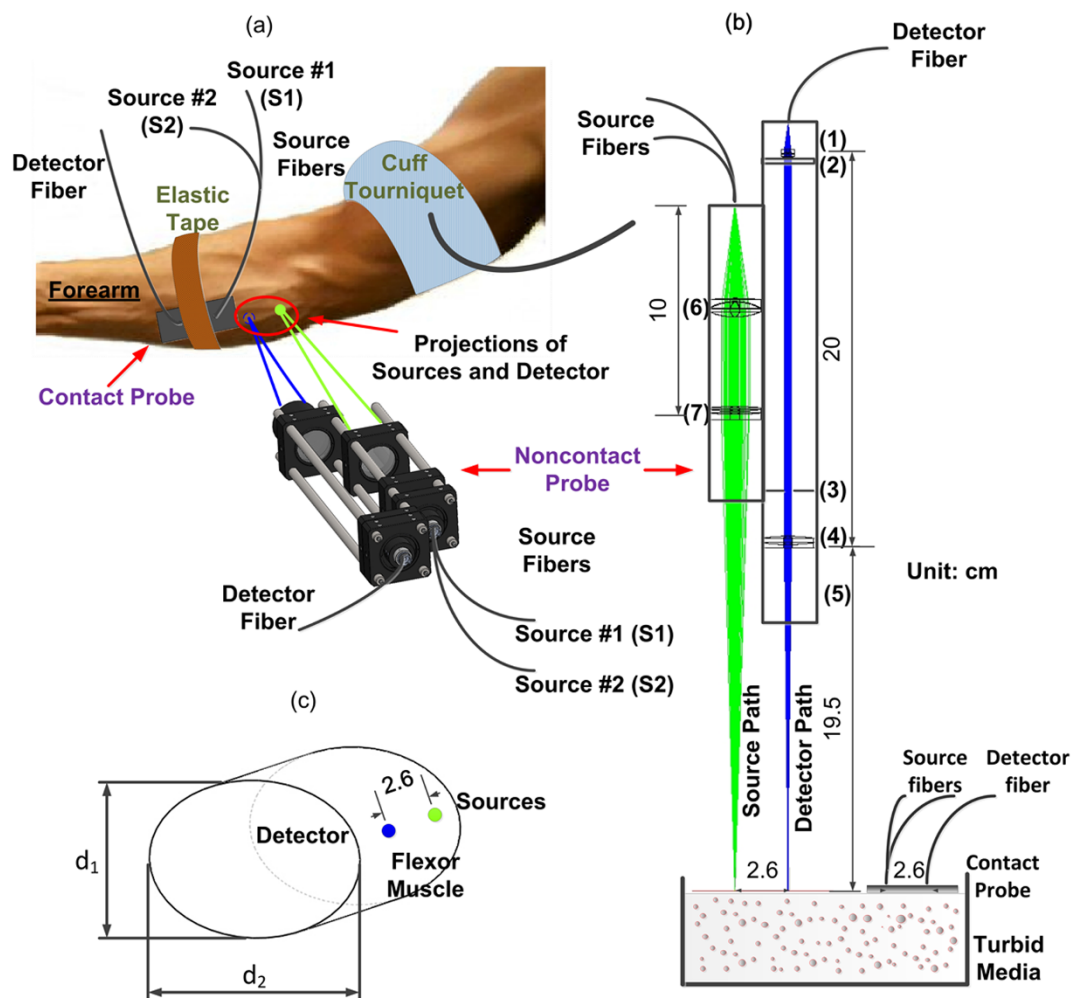


Figure 1 | Experimental configuration for concurrent measurements of rBF , $\Delta\mu_a$, $\Delta[HbO_2]$, and $\Delta[Hb]$ using both contact and noncontact probes in a forearm muscle (a) and a liquid phantom solution (b). The noncontact probe consisted of (1) collimator, (2) longpass optical filter (>750 nm), (3) aperture, (4) 20 cm focal length (FL) lens, (5) protection tube, (6) 5 cm FL lens, and (7) 25 cm FL lens. For evaluating the influence of arm curvature on noncontact measurements, the forearm was assumed as an elliptic cylinder with minor axis d_1 and major axis d_2 (c).

optical properties for the forearm ($\mu_a = 0.15 \text{ cm}^{-1}$ and $\mu_s' = 6.71 \text{ cm}^{-1}$ at 785 nm ; $\mu_a = 0.17 \text{ cm}^{-1}$ and $\mu_s' = 6.26 \text{ cm}^{-1}$ at 853 nm) and varied the dimensions of the elliptic cylinder ($d_1 = 5, 6, 7 \text{ cm}$; $d_2 = 4d_1/3$) in comparison to the semi-infinite geometry. With those assigned values above, the DPF_λ values at the two wavelengths were calculated based on either equation (6) for semi-infinite geometry or MC simulations for elliptic cylinders. The MC-simulated DPF_λ values for elliptic cylinders with different dimensions were then normalized (divided) by those derived from the analytical solution with semi-infinite geometry. The $\Delta[HbO_2]$ and $\Delta[Hb]$ were calculated from the normalized DPF_λ (Fig. 6a) based on equations (3–5) with an assumption (for simplicity) of equal $\Delta\mu_a$ at the two wavelengths. We evaluated the errors resulted from this assumption in phantom experimental data and found that the errors in the normalized DPF_λ were less than 2%, which can be ignored.

Figure 6a shows the normalized DPF_λ (DPF_λ ratios) at the two wavelengths and corresponding $\Delta[\text{oxygenation}]$ calculated from $\Delta[HbO_2]$ and $\Delta[Hb]$. The DPF_λ ratios ($\sim 80\%$) were significantly less than 1 ($p < 10^{-5}$), leading to $\sim 20\%$ underestimations of $\Delta[\text{oxygenation}]$.

Figure 6b shows that the elliptic cylinder curvature also induced $\sim 20\%$ underestimations in blood flow index (αD_B), as compared to the values calculated with semi-infinite geometry. However, the curvature influence on the relative change of αD_B (rBF) was very small ($< 1\%$, Fig. 6c), and can be ignored. More specifically, when

we created a αD_B variation (0.1×10^{-8} to 5×10^{-8} with an increment of 0.1×10^{-8}) for elliptic cylinder and semi-infinite geometries, the discrepancies in αD_B were observed (regression slope = 0.80, 0.81, 0.85 for $d_1 = 5, 6, 7 \text{ cm}$, respectively; Fig. 6b). However, no discrepancies in rBF were found (regression slope = 0.99, 1.00, 0.99 for $d_1 = 5, 6, 7 \text{ cm}$, respectively; Fig. 6c).

Overall, MC simulation results revealed that ignoring the curvature of the forearm would cause an underestimation in $\Delta[\text{oxygenation}]$, but not in rBF . These results are consistent with those obtained through *in vivo* muscle measurements described above.

Calibration of curvature effect. The underestimation of $\Delta[\text{oxygenation}]$ due to failure to consider the effect of forearm curvature can be calibrated using the corrected DPF_λ values calculated by the MC simulations with elliptic cylinder geometry. Figure 7 illustrates the calibration results in $\Delta[\text{oxygenation}]$. Calibration resulted in a substantial increase in the regression slope in each subject. On average, the calibrated regression slopes (0.56 ± 0.10 , $n = 10$) were significantly higher ($p < 10^{-3}$) than the original slopes without calibration (0.44 ± 0.12 , $n = 10$). Unlike the original slopes, the calibrated slopes were not correlated with the dimensions of the measured forearm: d_1 ($R^2 = 0.31$, $p = 0.10$) and d_2 ($R^2 = 0.28$, $p = 0.12$). This implied the efficiency of the calibration algorithm for reducing the curvature influence. The remaining

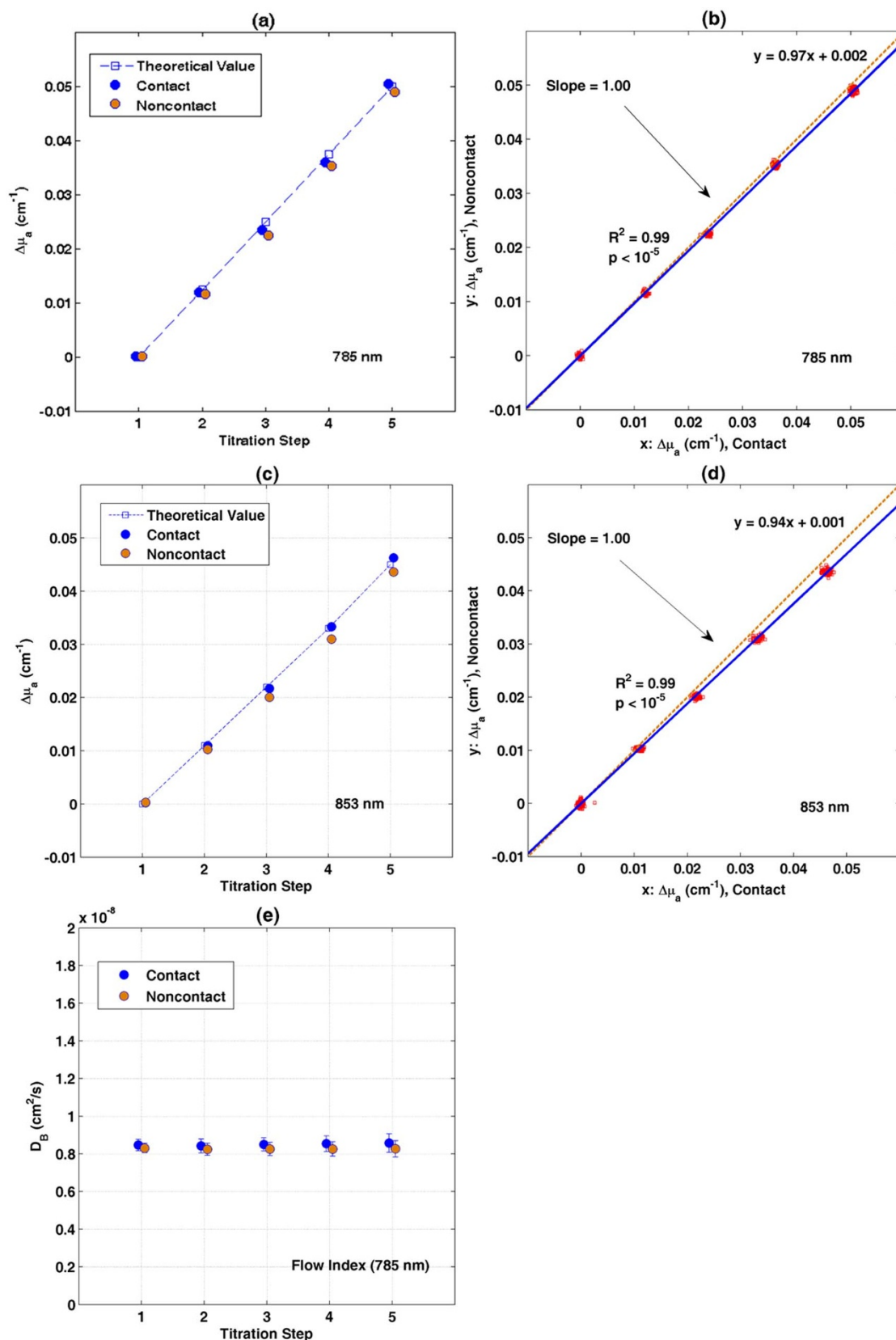


Figure 2 | Experimental results in tissue-like liquid phantom for comparisons of noncontact and contact measurements of $\Delta\mu_a$ and D_B . The raw data (150 data points at each titration step) for $\Delta\mu_a$ (a) and (c) and D_B (e) were averaged and displayed along with standard deviations (error bars). Notice that some error bars were too small to be observed. The $\Delta\mu_a$ values measured by both probes during ink titration agreed well with the theoretical values at the two wavelengths: 785 nm (a) and 853 nm (c). The noncontact and contact measurements of $\Delta\mu_a$ (i.e., 150 data points at each titration step) were significantly correlated at both wavelengths: (b) and (d). The flow indices (D_B) measured by both probes were almost constant throughout the titration steps (e).

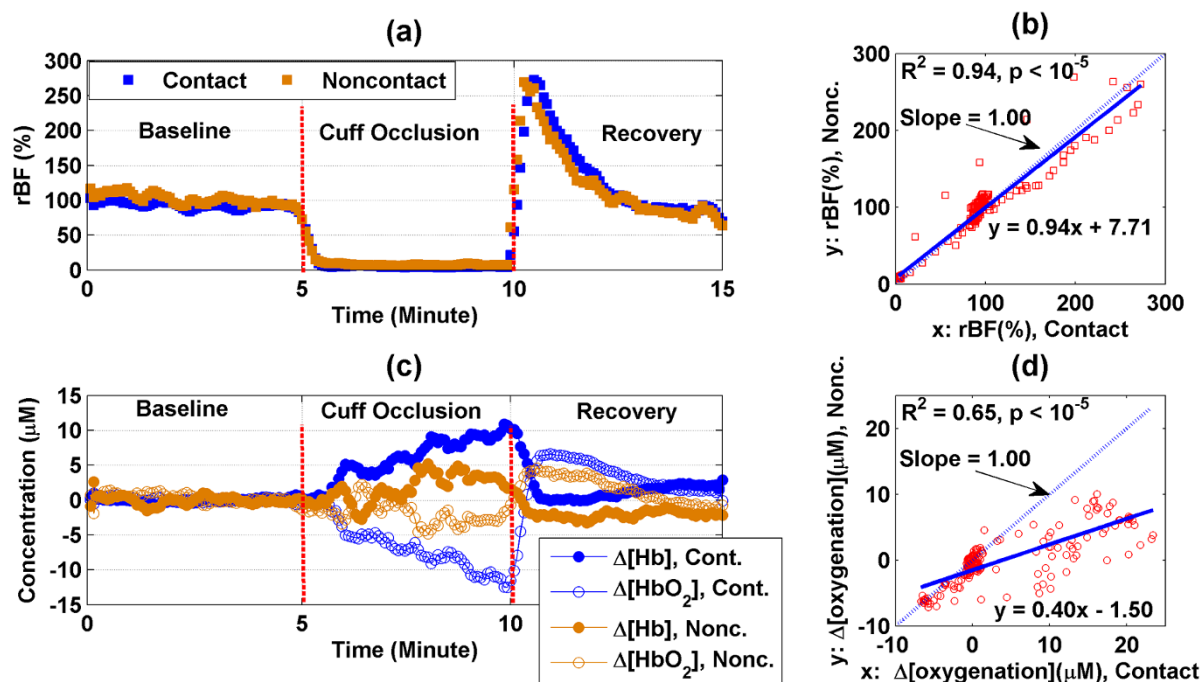


Figure 3 | Forearm muscle rBF (a) as well as $\Delta[Hb]$ and $\Delta[HbO_2]$ (c) responses during 5-minute arterial occlusion in one typical subject. Significant linear correlations between the contact and noncontact measurements of rBF (b) and $\Delta[oxygenation]$ (d) were observed although the regression slopes of rBF (0.94) and $\Delta[oxygenation]$ (0.40) were quite different.

discrepancy between the noncontact and contact measurements of $\Delta[oxygenation]$ (i.e., the calibrated regression slopes were still significantly smaller than 1) will be discussed in the next section.

Discussion

The newly developed dual-wavelength DCS flow-oximeter can simultaneously measure blood flow and blood oxygenation²³, thus providing deeper insight into tissue physiological status than either parameter alone. Previous studies with DCS flow-oximeter have measured tissue hemodynamics using fiber-optic probes placed on tissue surfaces^{23–29,40}, which may result in deformation of soft tissues (e.g., breast, muscle), thus distorting the measured tissue properties^{33–35}. The present study was designed to build and validate a noncontact dual-wavelength DCS flow-oximeter (Fig. 1) for simultaneous measurements of rBF and $\Delta[oxygenation]$ without physically touching the tissue. The noncontact system overcomes the contact limitations and is particularly powerful for longitudinal studies where repeatable measurements over time are needed³⁶.

This noncontact probe was compared against a contact probe in tissue-like liquid phantoms (Fig. 1b) and forearm muscles (Fig. 1a). The experimental results in liquid phantoms were very encouraging;

noncontact and contact measurements in both flow indices (D_B) and optical property changes ($\Delta\mu_a$) were highly consistent (Fig. 2). During the *in vivo* study, as expected, both rBF and $\Delta[oxygenation]$ responses in forearm muscles during cuff occlusion measured by the two probes were highly correlated (Fig. 3 and Fig. 4). The magnitudes of rBF responses measured by both probes were also highly consistent (Fig. 4a). Surprisingly, the magnitudes of $\Delta[oxygenation]$ measured by the noncontact probe were significantly lower than those measured by the contact probe (regression slope = 0.44 ± 0.12 , $n = 10$; Fig. 4b).

It should be noticed that the results discussed above (Fig. 2 to Fig. 4) were extracted using the analytical solutions for a homogeneous medium with semi-infinite geometry (equations (3–6)). These solutions have been broadly used to analyze the data obtained in contact measurements of blood flow and blood oxygenation^{16,18,19,21–23,25–29,31,32}. In fact, the contact probe (foam pad) secured by the elastic tape compressed the soft tissue of the forearm resulting in a flat tissue surface underneath the probe (approximating a semi-infinite geometry). By contrast, noncontact measurements did not change the shape of the forearm, which may be treated as an elliptic cylinder for simplicity (Fig. 1c). The fact that the regression slopes of

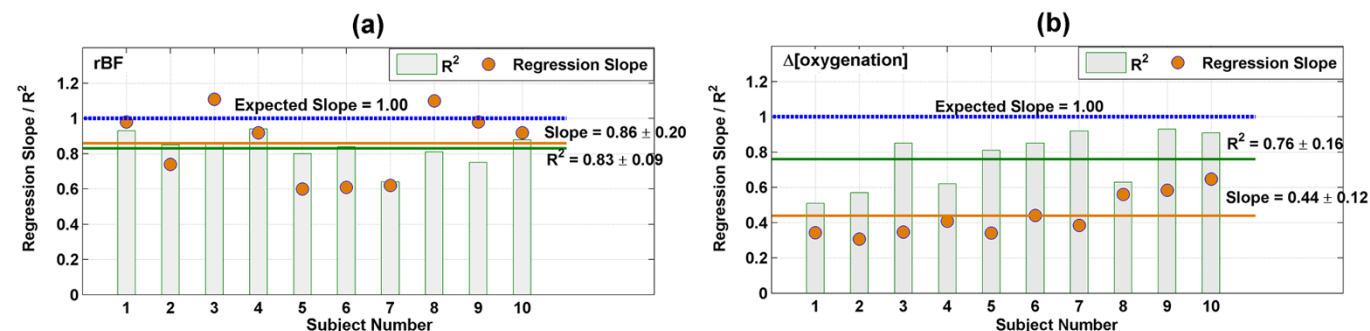


Figure 4 | Regression slopes and correlation coefficients between the contact and noncontact measurements in rBF (a) and $\Delta[oxygenation]$ (b) for the ten subjects.

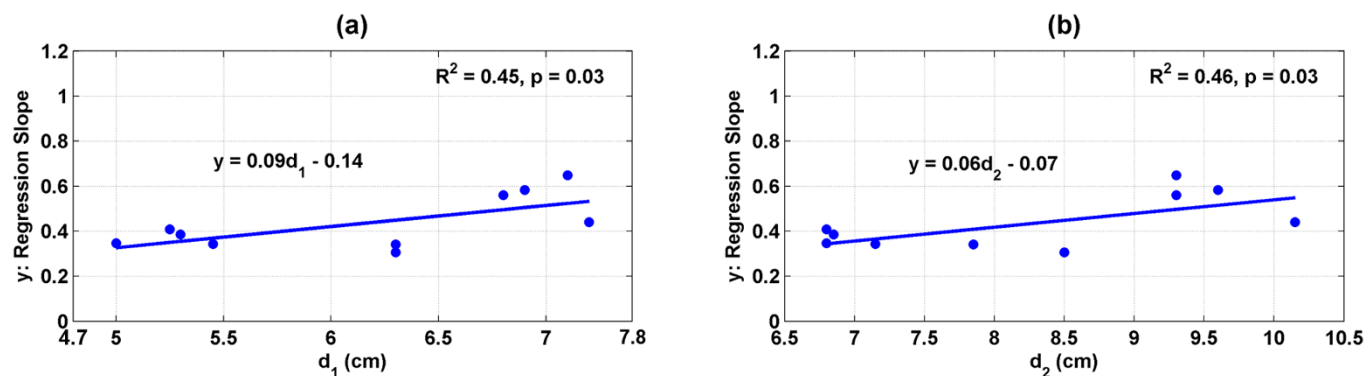


Figure 5 | Significant correlations between the regression slopes in $\Delta[\text{oxygenation}]$ and the dimensions of the forearm profile: d_1 (a) and d_2 (b).

$\Delta[\text{oxygenation}]$ were significantly correlated with the dimensions of the measured forearms (Fig. 5) implied the influence of forearm curvature on blood oxygenation measurements.

It is difficult to derive analytical solutions for irregular geometries such as the surface of an elliptic cylinder. MC simulations were thus used to investigate the forearm curvature influence. A series of elliptic cylinders with different dimensions mimicking the various shapes of forearms were examined for evaluation of the curvature influence on noncontact measurements. MC simulations demonstrated that the forearm curvature resulted in $\sim 20\%$ underestimations in $\Delta[\text{oxygenation}]$ (Fig. 6a) and αD_B (Fig. 6b), but had little effect on rBF (Fig. 6c). Similar underestimations in $\Delta[\text{oxygenation}]$ and αD_B yielded from the curvature-induced decrement of photon pathlengths in comparison to the semi-infinite geometry can be divided out when calculating the relative change of αD_B (rBF). Previous studies have also reported boundary/curvature effects on the quantification of tissue optical properties and blood oxygenation measurements^{49–52}, which are consistent with our findings.

Prompted by the finding of curvature influence, we attempted to correct the underestimation of noncontact measurements in $\Delta[\text{oxygenation}]$ resulting from the forearm curvature. Using the measured forearm dimensions and optical properties for each individual subject as input (Table 1), we performed the MC simulations to compute the DPF_λ , which was used to calculate $\Delta[\text{oxygenation}]$. The MC-calibrated regression slopes for $\Delta[\text{oxygenation}]$ (0.56 ± 0.10 , $n = 10$) were significantly higher than those (0.44 ± 0.12 , $n = 10$) computed using the DPF_λ calculated with semi-infinite geometry ignoring the curvature influence (Fig. 7). After calibration, the regression slopes were not correlated with the dimensions of the measured forearm, implying the calibration efficiency for reducing the curvature influence. It should be noted that considering the forearm as a simple elliptic cylinder may lead to evaluation errors. With the help of other 3-dimensional imaging modalities such as CT or MRI to characterize forearm curvature, the MC-based calibrations can be done more precisely.

The MC-based calibrations did not completely eliminate the discrepancy in $\Delta[\text{oxygenation}]$ between the noncontact and contact measurements in forearm muscles (i.e., the calibrated regression slope = $0.56 \pm 0.10 < 1$, $n = 10$). Furthermore, although it is insignificant ($p = 0.051$), the mean value of regression slopes for rBF (0.86 ± 0.20 , $n = 10$) was also smaller than 1 (Fig. 4a). Apparently, curvature influence was not the only factor causing the discrepancies between the two measurements in biological tissues.

The residual discrepancies between the noncontact and contact measurements may result from tissue heterogeneous responses as well as differences in measurement techniques (i.e., noncontact versus contact). Even though the regions measured by the two probes

were close (Fig. 1a), they did not completely overlap. The heterogeneity of muscle responses at different regions to arterial cuff occlusion may partially contribute to the discrepancies between the two measurements.

The noncontact probe may collect stray light in addition to the light reflected directly from forearm skin surface (without going through the deep muscle tissue). The stray light generates background noises and does not contain any dynamic information about tissue hemodynamics. Furthermore, previous studies have demonstrated that signals from different layers (cutaneous tissues and muscles) during arterial cuff occlusion were differentiated, revealing a strong hemodynamic response from the muscle¹⁹. Taken together, tissue hemodynamic responses during cuff occlusion measured by the noncontact probe may be underestimated.

On the other hand, the contact measurement may be influenced by imperfect coupling between the probe and tissue generating noises as well as the contact pressure distorting tissue hemodynamic responses. For example, researchers have observed more than twofold increases of muscle blood flow during application of external compression over a pressure range of 13–23 mmHg on human forearm³⁴ or 8–18 mmHg on human lower leg³³. The results were interpreted as an autoregulatory response following the decrease of the vascular transmural pressure gradient. Such local compression may also cause the redistribution of tissue blood oxygenation at the region around the contact probe, leading to more tissue heterogeneous responses. In addition, the probe contact compression may result in a decrease in adipose tissue thickness (ATT) over the flexor muscle, which may distort hemodynamic measurements.

The ATT influence is another concern with NIRS measurements^{53,54}. The penetration depth of NIR light in biological tissues is known to be roughly half of the S-D separation⁵⁵. An S-D separation of 2.6 cm was used for the present study, probing a depth of ~ 1.3 cm. Previous studies have shown that for an S-D separation of 2 cm or greater, the contribution of skin is less than 5% of total light absorption, and the detected signal is mainly from skeletal muscle tissues⁵⁶. The results imply that the sensitivity of the NIRS/DCS signal detected with an S-D separation of 2.6 cm should not be significantly affected by the ATT observed in our study (0.37 ± 0.06 cm, $n = 10$; Table 1). Furthermore, no significant correlations were observed between ATT and rBF or ATT and $\Delta[\text{oxygenation}]$ in this study, implying that ATT did not adversely influence our measurements. There have been studies correcting the variation in measurement sensitivity due to ATT based on Monte Carlo simulations⁵⁷, which may be employed in future work with subjects that have significant ATT .

In conclusion, we report a novel noncontact dual-wavelength DCS flow-oximeter for simultaneous measurement of blood flow and blood oxygenation in deep tissues. This noncontact detection system is unique in that its source and detector paths built by optical lenses

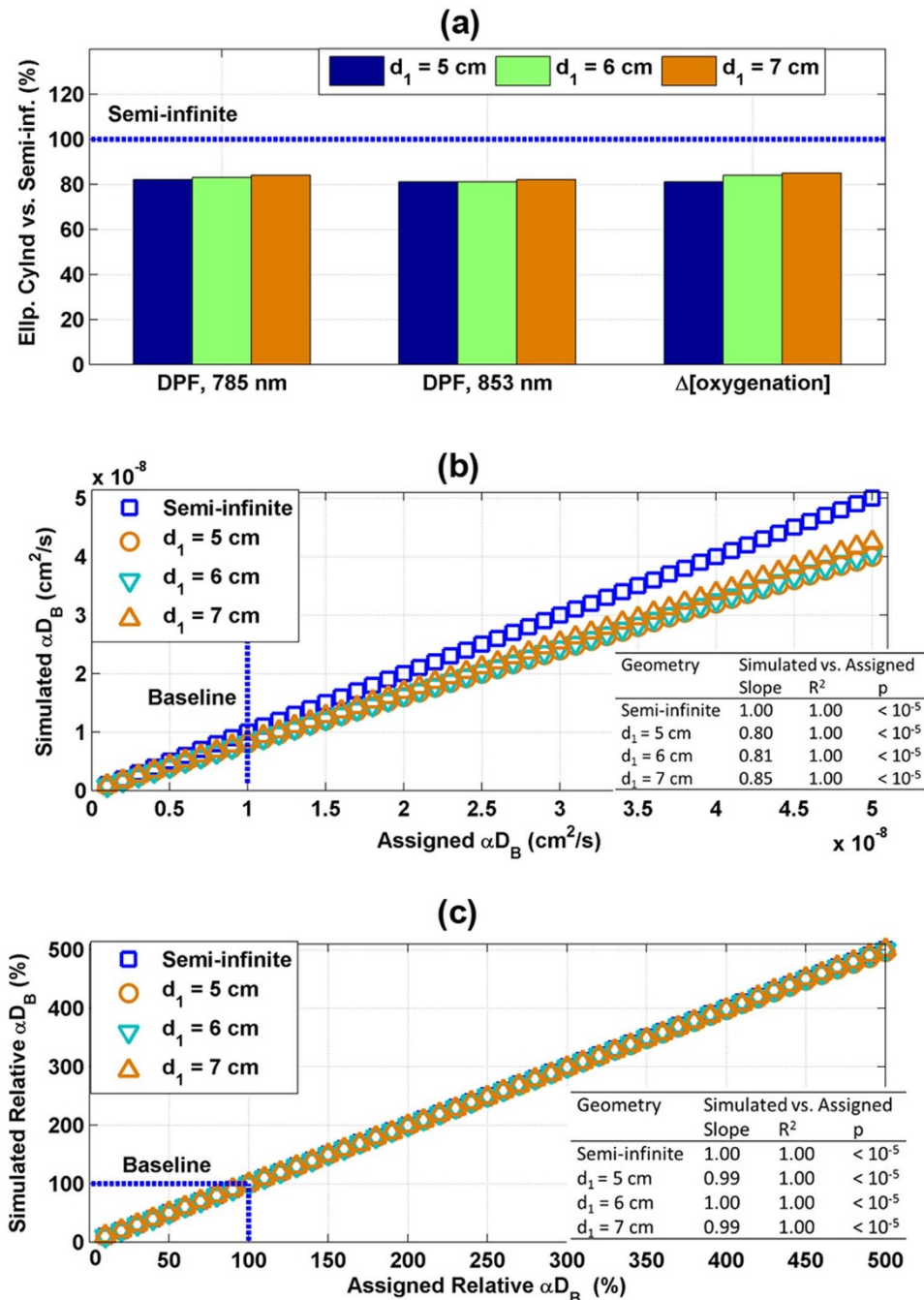


Figure 6 | Monte Carlo simulation results for evaluation of forearm curvature influence on optical measurements. Ignoring the forearm curvature caused underestimations in DPF_{λ} and $\Delta[\text{oxygenation}]$ (a) and αD_B (b), but did not affect rBF (c).

are completely separated/isolated, which avoids the interference between the source and detector and enables a large source-detector distance for deep tissue measurements. The noncontact probe has been compared with a contact probe in tissue-like phantoms and forearm muscles. The dynamic trends in both flow and oxygenation changes in forearm muscles measured by the two probes were found to be highly correlated. Compared to the contact measurements, however, the magnitudes of blood oxygenation changes measured by the noncontact probe were significantly lower. Monte Carlo simulations and tissue-like phantom experiments confirmed that ignoring the forearm curvature caused a significant underestimation of oxygenation changes, which can be corrected using a calibration algorithm based on the MC simulation. However, the curvature influence was not the only factor causing the discrepancies between the

noncontact and contact measurements in tissue blood oxygenation. Further comparisons with other established technologies for tissue blood flow and oxygenation measurements are needed to identify other possible factors (such as tissue heterogeneous responses and differences in measurement techniques) that may cause the residual discrepancies between the two measurements. Nevertheless, our research paves the way for simultaneous and noncontact monitoring of blood flow and oxygenation in soft (e.g., breast, muscle) and vulnerable (e.g., ulcerous) tissues without distorting tissue hemodynamics.

Methods

Instrumentation. *DCS flow-oximeter.* The dual-wavelength DCS flow-oximeter has been described in detail elsewhere³⁶. Briefly, two continuous-wave (CW) long-

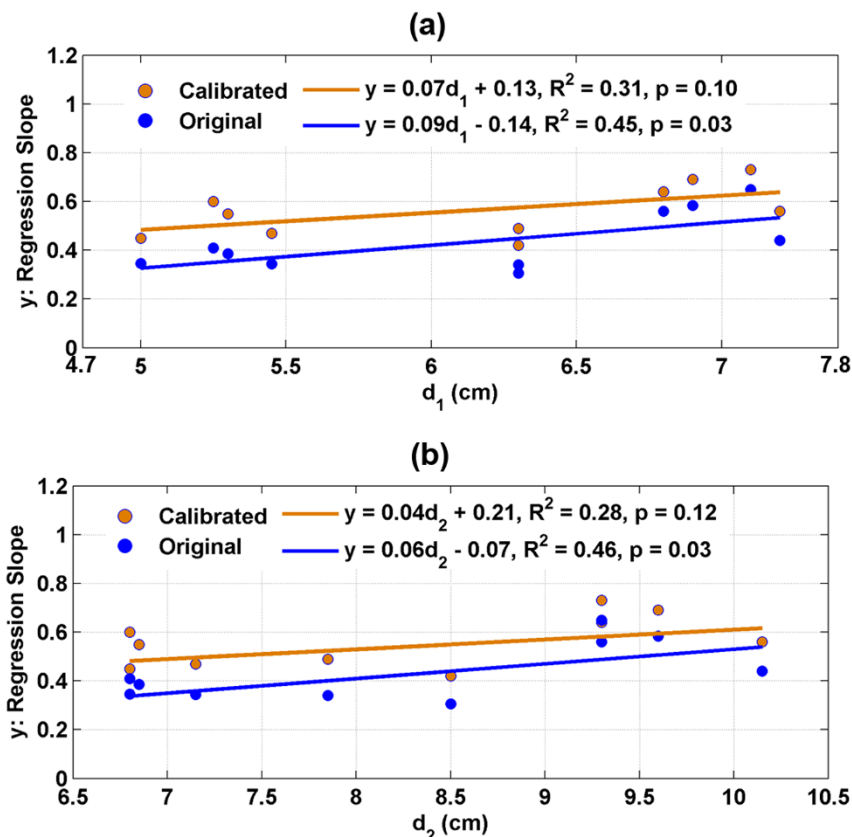


Figure 7 | Calibration results in $\Delta[\text{oxygenation}]$. The MC-based calibration resulted in significant increases in regression slopes of noncontact versus contact measurements. After calibration, the regression slopes were significantly increased and not correlated with the dimensions of the measured forearm d_1 (a) and d_2 (b), indicating the reduction of curvature influence on $\Delta[\text{oxygenation}]$.

coherence (> 5 meters, Crystalaser, NV, USA) lasers at wavelengths of 785 and 853 nm emit light alternatively into the tissue via two multimode source fibers (WF200/220/245, Ceramoptec, MA, USA) bundled together. Photons transport through tissues, and only some of them are collected by a single-mode detector fiber (SM800, Fibertec, CA, USA) placed on the tissue surface at a distance of several millimeters or centimeters from the source fibers. The detector fiber is connected to a single-photon-counting avalanche photodiode (APD, PerkinElmer, Canada) which detects photons from a single speckle area on the tissue surface. The APD outputs are fed into a correlator board (correlator.com, NJ, USA) to compute the light intensity and intensity temporal autocorrelation function³⁶. The sampling rate of the dual-wavelength DCS flow-oximeter is 0.4 Hz.

Blood flow index is extracted by fitting the normalized electric field autocorrelation function $g_1(\vec{r}, \tau) = G_1(\vec{r}, \tau) / G_1(\vec{r}, 0)$ calculated from the measured light intensity autocorrelation function $g_2(\vec{r}, \tau) = \langle I(\vec{r}, t) I(\vec{r}, t + \tau) \rangle / \langle I \rangle^2$ through Siegert relation³⁸. Here $I(\vec{r}, t)$ is the detected light intensity at position \vec{r} and time t , $\langle \dots \rangle$ denotes a time average, and τ is the autocorrelation delay time. The electric field temporal autocorrelation function $G_1(\vec{r}, \tau)$ satisfies the correlation diffusion equation in highly scattering media^{14,16,19,37}:

$$\left(D\nabla^2 - v\mu_a - \frac{1}{3}v\mu_s'k_0^2\alpha\langle\Delta r^2(\tau)\rangle \right) G_1(\vec{r}, \tau) = -vS(\vec{r}) \quad (1)$$

Where μ_a is medium absorption coefficient, μ_s' is reduced scattering coefficient, $D = v/3\mu_s'$ is the photon diffusion coefficient, v is light speed in the media, k_0 is the wavenumber, $S(\vec{r})$ is the source light distribution, α is defined as the ratio of moving scatterers to total scatterers, and $\langle\Delta r^2(\tau)\rangle$ is the mean-square displacement of moving scatterers (e.g., RBCs) at time τ . The homogeneous CW solution to equation (1) for a semi-infinite geometry is¹⁶:

$$G_1(\rho, \tau) = \frac{vS_0}{4\pi D} \left(\frac{\exp(-K(\tau)r_1)}{r_1} - \frac{\exp(-K(\tau)r_2)}{r_2} \right) \quad (2)$$

Here ρ is the source-detector (S-D) separation, S_0 is source intensity, $K^2(\tau) = 3\mu_a\mu_s' + \mu_s'^2k_0^2\alpha\langle\Delta r^2(\tau)\rangle$, $r_1 = [\rho^2 + (z - z_0)^2]^{1/2}$, $r_2 = [\rho^2 + (z + z_0 + 2z_b)^2]^{1/2}$, $z_0 = 1/\mu_s'$, $z_b = 2(1 + R_{\text{eff}})/3(1 - R_{\text{eff}})$, $R_{\text{eff}} = -1.440n^{-2} + 0.710n^{-1} + 0.668 + 0.064n$, and $n \approx 1.34$ is the ratio of refractive indices between the medium and air.

The exact form of equation (1) depends on the nature and heterogeneity of scatterers' motion. The widely used diffusion model was originally applied in highly

scattering media such as colloidal suspensions or Intralipid solutions wherein the dynamics is Brownian motion of scatterers^{14,39}. For this case, $\langle\Delta r^2(\tau)\rangle = 6D_B\tau$, where D_B is the Brownian diffusion coefficient of moving scatterers^{14,40}. Interestingly, it has been observed that the diffusion model fits the autocorrelation curves well over a broad range of tissue types^{18,20,28,31,32}. The combined term, αD_B , is referred to as blood flow index (BFI) in biological tissues and is commonly used to calculate rBF (i.e., $BFI(t)/BFI_{\text{baseline}}$). In general, biological tissues contain relatively static scatterers (e.g., mitochondria) and dynamic scatterers (e.g., RBCs). The signals scattered from the static scatterers do not contribute significantly to the temporal decay of the autocorrelation function. To account for this effect, a unitless factor, α , is introduced to represent the fraction of light scattering events from dynamic scatterers. In contrast to biological tissues, all scatterers (Intralipid particles) in the liquid phantom are dynamic and contribute significantly to the temporal decay of the autocorrelation function, resulting in $\alpha = 1$. Accordingly, the flow index of the liquid phantom is reported as simply D_B .

Blood oxygenation variations ($\Delta[HbO_2]$ and $\Delta[Hb]$) are obtained from the measured light intensity changes at the two wavelengths ($\lambda_1 = 785$ nm and $\lambda_2 = 853$ nm) using the modified Beer-Lambert law²³:

$$\Delta\mu_a(\lambda) = \ln \left(\frac{I_{TB}}{I_{TB}} \right) / \rho \text{DPF}_\lambda \quad (3)$$

$$\Delta[HbO_2] = \frac{\varepsilon_{Hb}(\lambda_1)\Delta\mu_a(\lambda_2) - \varepsilon_{Hb}(\lambda_2)\Delta\mu_a(\lambda_1)}{\varepsilon_{Hb}(\lambda_1)\varepsilon_{HbO_2}(\lambda_2) - \varepsilon_{HbO_2}(\lambda_1)\varepsilon_{Hb}(\lambda_2)} \quad (4)$$

$$\Delta[Hb] = \frac{\varepsilon_{HbO_2}(\lambda_2)\Delta\mu_a(\lambda_1) - \varepsilon_{HbO_2}(\lambda_1)\Delta\mu_a(\lambda_2)}{\varepsilon_{Hb}(\lambda_1)\varepsilon_{HbO_2}(\lambda_2) - \varepsilon_{HbO_2}(\lambda_1)\varepsilon_{Hb}(\lambda_2)} \quad (5)$$

Where $\Delta\mu_a(\lambda)$ is the relative change of μ_a at wavelength λ . I_{TB} and I_{TT} are the measured light intensities at the baseline (B) and at time T, respectively. $\varepsilon_{HbO_2}(\lambda)$ and $\varepsilon_{Hb}(\lambda)$ are the extinction coefficients of HbO_2 and Hb , respectively. The differential pathlength factor (DPF_λ) is the ratio of mean photon pathlength over the S-D separation (ρ), which can be calculated from the measured μ_a and $\mu_s'^{8,41}$:

$$\text{DPF}_\lambda = \frac{3\mu_s'(\lambda)\rho}{2(1 + \rho\sqrt{3\mu_s'(\lambda)\mu_a(\lambda)})} \quad (6)$$

Fiber-optic probes. Figure 1 shows a schematic of the noncontact and contact probes for DCS flow-oximeter and experimental setup for *in vivo* (Fig. 1a) and phantom



(Fig. 1b) measurements. Compared to our previous noncontact probe design for DCS blood flow measurements³⁶, the only difference was to bundle a second source fiber (S2) to the original source fiber (S1) and connect the two source fibers to the dual-wavelength DCS flow-oximeter. Again, the noncontact probe was designed using two isolated optical paths consisted of lenses and collimators for source and detector respectively (Fig. 1a and Fig. 1b). This unique design avoided the interference between the source and detector paths and enabled the setting of large S-D separations (e.g., 2.6 cm, used in this study) for deep tissue measurements³⁶. The noncontact measurements were compared with the contact measurements conducted by a contact probe (Fig. 1a and Fig. 1b) with an identical S-D separation (2.6 cm) confined in their positions by a black foam pad. The foam pad was placed on the surface of the measured tissue (Fig. 1a) or liquid phantom (Fig. 1b) using elastic tape or a custom-made holder³⁶. Room light was turned off during measurements.

Experimental protocols. Tissue-like liquid phantom. Tissue-like liquid phantoms, comprised of Intralipid, distilled water and India ink, have been extensively used for NIRS/DCS calibrations^{36,40}. Intralipid particles (Fresenius Kabi, Sweden) provide the control of scattering (μ_s') and Brownian motion (D_B) while India ink (10% of Black India 44201, Higgins, MA, USA) provides the control of absorption (μ_a). We set a constant μ_s' (10 cm^{-1}) and varied μ_a (0.0500, 0.0625, 0.0750, 0.0875, 0.1000 cm^{-1} at 785 nm) by adding ink to compare the $\Delta\mu_a$ results measured by the noncontact and contact probes. The $\Delta\mu_a$ range was set based on the realistic changes in forearm muscles that we measured during cuff occlusion. Approximate six-minute data (150 data points) were collected and averaged at each titration step. Although temperature can affect Brownian motions (D_B) of Intralipid particles, the room temperature was controlled constant ($\sim 23^\circ \text{C}$) in order to obtain stable flow. The tissue-like phantom provides an ideal homogeneous tissue model with semi-infinite geometry (flat surface) for testing the noncontact and contact measurements.

In vivo human muscle. With signed Institutional Review Board approval consents, 10 healthy volunteers participated in the experiments. The subject lay supine and extended right forearm. The adipose tissue thickness (ATT) over the forearm flexor muscle was measured using a skinfold caliper (Lange 85300, Texas, USA). For evaluating the influence of forearm curvature on optical measurements, we simply assumed the forearm as an elliptic cylinder with minor axis d_1 and major axis d_2 (Fig. 1c). The d_1 and d_2 for each individual were measured using a vernier caliper. A hand-held fiber-optic contact probe connected to a commercial frequency-domain NIRS system (Imagent, ISS Inc. IL, USA) was used to quantify the absolute baseline values of μ_a and μ_s' in the forearm muscle³⁶, which were used to calculate the DPF_s values (equation (6)) and rBF (equation (2)) for each subject.

The noncontact and contact probes were then configured (Fig. 1a) to detect hemodynamic changes in forearm flexor muscle during arterial cuff occlusion, generated by an automatic tourniquet placed on the upper arm. The total protocol included 5-minute resting baseline, 5-minute arterial cuff occlusion (230 mmHg) and 5-minute recovery measurement following the release of occlusion.

Monte Carlo simulation. The algorithms described above simply assume the tissue as a homogenous medium with semi-infinite geometry (flat surface), which yields an analytical solution (equation (2)) or a simple expression (equation (3)). The approximation of semi-infinite geometry might be appropriate for the contact measurements as the soft tissue underneath the foam pad becomes flat due to the compression by the elastic tape. However, this approximation does not work for the noncontact measurements where the forearm curvature cannot be ignored. To evaluate such influence, the forearm muscle was simply treated as a homogeneous tissue with curved surface on an elliptic cylinder. Monte Carlo (MC) simulations^{42,43} were performed on the geometry of elliptic cylinder with varied dimensions (i.e., d_1 and d_2) in comparison to the results with semi-infinite geometry.

For MC simulations, an established program simulating photon propagation in an arbitrary geometry with 3-dimensional spatial varying optical properties^{44,45} was used to compute total pathlengths of the photons captured by the detector. For each simulation, 10 million photons were launched into the tissue to achieve a sufficient signal-to-noise ratio^{13,43,44}.

For the evaluation of flow measurements, the normalized electric field temporal autocorrelation was generated from the detected photon pathlengths (s)⁴⁶:

$$g_1(\tau) = \int_0^\infty P(s) \exp\left(-\frac{1}{3}k_0^2 \alpha (\Delta r^2(\tau)) \frac{s}{l^*}\right) ds \quad (7)$$

Where $P(s)$ is the histogram of detected photon pathlengths (s) and l^* is the photon random walk step length, which is equal to $1/\mu_s'$. As mentioned above, $\langle \Delta r^2(\tau) \rangle = 6D_B\tau$. Using equation (7) and assigning a value of αD_B , we obtained a simulated $g_1(\tau)$. We then fitted this $g_1(\tau)$ using the algorithm for semi-infinite geometry (equation (2)) to extract the flow index for comparisons.

For the evaluation of blood oxygenation measurements, the DPF_s was calculated by dividing the mean photon pathlength by the S-D separation (2.6 cm). The lengths of the photon paths through the tissue were weighted by the detected intensities and were accumulated to calculate the mean photon pathlength^{13,47,48}. We then compared the differences in blood oxygenation resulted from the different DPF_s calculated with different geometries.

Data analysis. For simplicity, we reduced the two oxygenation quantities to one and named it as “ $\Delta[\text{oxygenation}]$ ” (i.e., $\Delta[\text{oxygenation}] = \Delta[\text{HbO}_2] - \Delta[\text{Hb}]$)³⁰. Since DCS flow signals are not sensitive to wavelength, we reported flow data with only one

wavelength (785 nm)^{23,40}. Linear regression analyses were carried out in each individual for evaluating the correlation/consistency of the contact and noncontact measurements. The regression slope, correlation coefficient, and p-value were reported for each subject. Ideally, the regression slope should be equal to 1 if the two measurements were consistent. Two-tailed Student t-test was used to test the consistency between the two measurements (i.e., whether the regression slope is statistically equal to 1), $p < 0.05$ was considered significant. All statistical results were presented as mean \pm standard deviation (*s.d.*).

- Barth, M. *et al.* Correlation of Clinical Outcome with Pressure-, Oxygen-, and Flow-Related Indices of Cerebrovascular Reactivity in Patients Following Aneurysmal SAHs. *Neurocrit. Care* **12**, 234–243 (2010).
- Caprara, C. & Grimm, C. From oxygen to erythropoietin: Relevance of hypoxia for retinal development, health and disease. *Prog. Retin. Eye Res.* **31**, 89–119 (2012).
- Dostanic, M. *et al.* New trends in neuromonitoring patients with with aneurysmal subarachnoid haemorrhage. *Acta. Chir. Iugosl.* **55**, 69–74 (2008).
- Edul, V. S. K., Dubin, A. & Ince, C. The Microcirculation as a Therapeutic Target in the Treatment of Sepsis and Shock. *Sem. Resp. Crit. Care Med* **32**, 558–568 (2011).
- Schober, P. & Schwarte, L. A. From system to organ to cell: oxygenation and perfusion measurement in anesthesia and critical care. *J. Clin. Monit. Comput* **26**, 255–265 (2012).
- White, S. M. *et al.* Longitudinal In Vivo Imaging to Assess Blood Flow and Oxygenation in Implantable Engineered Tissues. *Tissue Engineering Part C-Meth.* **18**, 697–709 (2012).
- Wolf, U. *et al.* Localized irregularities in hemoglobin flow and oxygenation in calf muscle in patients with peripheral vascular disease detected with near-infrared spectrophotometry. *J. Vasc. Surg.* **37**, 1017–1026 (2003).
- Fantini, S. *et al.* Non-invasive optical monitoring of the newborn piglet brain using continuous-wave and frequency-domain spectroscopy. *Phys. Med. Biol.* **44**, 1543–1563 (1999).
- Gagnon, R. E., Macnab, A. J., Gagnon, F. A., Blackstock, D. & LeBlanc, J. G. Comparison of two spatially resolved NIRS oxygenation indices. *J. Clin. Monit. Comput* **17**, 385–391 (2002).
- Jöbsis, F. F. Noninvasive, infrared monitoring of cerebral and myocardial oxygen sufficiency and circulatory parameters. *Science* **198**, 1264–1267 (1977).
- Ferrari, M., Muthalib, M. & Quaresima, V. The use of near-infrared spectroscopy in understanding skeletal muscle physiology: recent developments. *Philos. Transact. A Math. Phys. Eng. Sci.* **369**, 4577–4590 (2011).
- Hamaoka, T., McCully, K. K., Niwayama, M. & Chance, B. The use of muscle near-infrared spectroscopy in sport, health and medical sciences: recent developments. *Philos. Transact. A Math. Phys. Eng. Sci.* **369**, 4591–4604 (2011).
- Li, T., Gong, H. & Luo, Q. Visualization of light propagation in visible Chinese human head for functional near-infrared spectroscopy. *J. Biomed. Opt.* **16**, 045001 (2011).
- Pine, D. J., Weitz, D. A., Chaikin, P. M. & Herbolzheimer, E. Diffusing wave spectroscopy. *Phys. Rev. Lett.* **60**, 1134–1137 (1988).
- Boas, D. A., Campbell, L. E. & Yodh, A. G. Scattering and Imaging with Diffusing Temporal Field Correlations. *Phys. Rev. Lett.* **75**, 1855–1858 (1995).
- Cheung, C., Culver, J. P., Takahashi, K., Greenberg, J. H. & Yodh, A. G. In vivo cerebrovascular measurement combining diffuse near-infrared absorption and correlation spectroscopies. *Phys. Med. Biol.* **46**, 2053 (2001).
- Culver, J. P. *et al.* Diffuse optical tomography of cerebral blood flow, oxygenation, and metabolism in rat during focal ischemia. *J. Cerebr. Blood F. Met* **23**, 911–924 (2003).
- Durduran, T. *et al.* Diffuse optical measurement of blood flow in breast tumors. *Opt. Lett.* **30**, 2915–2917 (2005).
- Yu, G. *et al.* Time-dependent blood flow and oxygenation in human skeletal muscles measured with noninvasive near-infrared diffuse optical spectroscopies. *J. Biomed. Opt.* **10**, 024027 (2005).
- Yu, G. *et al.* Noninvasive monitoring of murine tumor blood flow during and after photodynamic therapy provides early assessment of therapeutic efficacy. *Clin. Cancer Res.* **11**, 3543–3552 (2005).
- Durduran, T. *et al.* Diffuse optical measurement of blood flow, blood oxygenation, and metabolism in a human brain during sensorimotor cortex activation. *Opt. Lett.* **29**, 1766–1768 (2004).
- Kim, M. N. *et al.* Noninvasive measurement of cerebral blood flow and blood oxygenation using near-infrared and diffuse correlation spectroscopies in critically brain-injured adults. *Neurocrit. Care* **12**, 173–180 (2010).
- Shang, Y. *et al.* Portable optical tissue flow oximeter based on diffuse correlation spectroscopy. *Opt. Lett.* **34**, 3556–3558 (2009).
- Shang, Y., Chen, L., Toborek, M. & Yu, G. Diffuse optical monitoring of repeated cerebral ischemia in mice. *Opt. Express* **19**, 20301–20315 (2011).
- Shang, Y. *et al.* Cerebral monitoring during carotid endarterectomy using near-infrared diffuse optical spectroscopies and electroencephalogram. *Phys. Med. Biol.* **56**, 3015 (2011).
- Yu, G. *et al.* Intraoperative evaluation of revascularization effect on ischemic muscle hemodynamics using near-infrared diffuse optical spectroscopies. *J. Biomed. Opt.* **16**, 027004 (2011).
- Cheng, R., Shang, Y., Hayes, D. Jr., Saha, S. P. & Yu, G. Noninvasive optical evaluation of spontaneous low frequency oscillations in cerebral hemodynamics. *Neuroimage* **62**, 1445–1454 (2012).



28. Dong, L. *et al.* Noninvasive diffuse optical monitoring of head and neck tumor blood flow and oxygenation during radiation delivery. *Biomed. Opt. Express* **3**, 259–272 (2012).
29. Yu, G. Near-infrared diffuse correlation spectroscopy in cancer diagnosis and therapy monitoring. *J. Biomed. Opt.* **17**, 010901–010901 (2012).
30. Izzetoglu, M., Bunce, S. T., Izzetoglu, K., Onaral, B. & Pourrezaei, K. Functional Brain Imaging Using Near-Infrared Technology. *Ieee. Eng. Med. Biol.* **7**, 38–46 (2007).
31. Zhou, C. *et al.* Diffuse optical monitoring of blood flow and oxygenation in human breast cancer during early stages of neoadjuvant chemotherapy. *J. Biomed. Opt.* **12**, 051903–051903 (2007).
32. Gurley, K., Shang, Y. & Yu, G. Noninvasive optical quantification of absolute blood flow, blood oxygenation, and oxygen consumption rate in exercising skeletal muscle. *J. Biomed. Opt.* **17**, 075010–075011 (2012).
33. Lawrence, D. & Kakkar, V. V. Graduated, static, external compression of the lower limb: a physiological assessment. *Br. J. Surg.* **67**, 119–121 (1980).
34. Bochmann, R. P. *et al.* External compression increases forearm perfusion. *J. Appl. Physiol.* **99**, 2337–2344 (2005).
35. Dai, G., Gertler, J. P. & Kamm, R. D. The effects of external compression on venous blood flow and tissue deformation in the lower leg. *J. Biomech. Eng.* **121**, 557–564 (1999).
36. Lin, Y., He, L., Shang, Y. & Yu, G. Noncontact diffuse correlation spectroscopy for noninvasive deep tissue blood flow measurement. *J. Biomed. Opt.* **17**, 010502 (2012).
37. Yu, G. *et al.* Validation of diffuse correlation spectroscopy for muscle blood flow with concurrent arterial spin labeled perfusion MRI. *Opt. Express* **15**, 1064–1075 (2007).
38. Rice, S. O. "Mathematical analysis of random noise and stochastic process," in *Mathematical analysis of random noise and stochastic process*, p. 133, Dover, New York (1954).
39. Maret, G. & Wolf, P. E. Multiple light scattering from disordered media: the effect of Brownian motion of scatterers. *Z. Phys. B* **65**, 409–413 (1987).
40. Irwin, D. *et al.* Influences of tissue absorption and scattering on diffuse correlation spectroscopy blood flow measurements. *Biomed. Opt. Express* **2**, 1969–1985 (2011).
41. Shao, J., Lin, L., Niwayama, M., Kudo, N. & Yamamoto, K. Theoretical and experimental studies on linear and nonlinear algorithms for the measurement of muscle oxygenation using continuous-wave near-infrared spectroscopy. *Opt. Eng.* **40**, 2293–2301 (2001).
42. Jacques, S. L. & Wang, L. "Monte Carlo modeling of light transport in tissues," in *Optical-Thermal response of laser-irradiated tissue* W. a. v. Gemert, Ed., pp. 73–100, A. J. Welch and v. Gemert, Plenum, New York (1995).
43. Wang, L., Jacques, S. L. & Zheng, L. MCML--Monte Carlo modeling of light transport in multi-layered tissues. *Comput. Methods Programs Biomed.* **47**, 131–146 (1995).
44. Boas, D., Culver, J., Stott, J. & Dunn, A. Three dimensional Monte Carlo code for photon migration through complex heterogeneous media including the adult human head. *Opt. Express* **10**, 159–170 (2002).
45. Li, T., Gong, H. & Luo, Q. MCV: Monte Carlo modeling of photon migration in voxelized media. *J. Innovative Opt. Health Sci.* **03**, 91–102 (2010).
46. Boas, D. A. Diffuse photon probes of structural and dynamical properties of turbid media: theory and biomedical applications. *PhD diss., University of Pennsylvania* (1996).
47. Fukui, Y., Ajichi, Y. & Okada, E. Monte Carlo Prediction of Near-Infrared Light Propagation in Realistic Adult and Neonatal Head Models. *Appl. Opt.* **42**, 2881–2887 (2003).
48. Okada, E. & Delpy, D. T. Near-infrared light propagation in an adult head model. I. Modeling of low-level scattering in the cerebrospinal fluid layer. *Appl. Opt.* **42**, 2906–2914 (2003).
49. Fantini, S., Franceschini, M., Fishkin, J. B., Barbieri, B. & Gratton, E. Quantitative determination of the absorption spectra of chromophores in strongly scattering media: a light-emitting-diode based technique. *Appl. Opt.* **33**, 5204–5213 (1994).
50. Mantulin, W. W. *et al.* Tissue optical parameter map generated with frequency-domain spectroscopy. *Proc. of SPIE* **2396**, 323–330 (1995).
51. Franceschini, M. A. *et al.* Frequency-domain techniques enhance optical mammography: initial clinical results. *P. Natl. Acad. Sci. USA* **94**, 6468–6473 (1997).
52. Tuchin, V. V. *Tissue Optics: Light Scattering Methods and Instruments for Medical Diagnosis*, second edition. *SPIE Press, Bellingham, WA*, 480–482 (2007).
53. Yang, Y., Soyemi, O. O., Landry, M. R. & Soller, B. R. Influence of a fat layer on the near infrared spectra of human muscle: quantitative analysis based on two-layered Monte Carlo simulations and phantom experiments. *Opt. Express* **13**, 1570–1579 (2005).
54. Sayli, O., Aksel, E. B. & Akin, A. Crosstalk and error analysis of fat layer on continuous wave near-infrared spectroscopy measurements. *J. Biomed. Opt.* **13**, 064019 (2008).
55. van Beekvelt, M. C. P., Colier, W., Wevers, R. A. & van Engelen, B. G. M. Performance of near-infrared spectroscopy in measuring local O₂ consumption and blood flow in skeletal muscle. *J. Appl. Physiol.* **90**, 511–519 (2001).
56. Hampson, N. B. & Piantadosi, C. A. Near infrared monitoring of human skeletal muscle oxygenation during forearm ischemia. *J. Appl. Physiol.* **64**, 2449–2457 (1988).
57. Niwayama, M., Lin, L., Shao, J., Kudo, N. & Yamamoto, K. Quantitative measurement of muscle hemoglobin oxygenation using near-infrared spectroscopy with correction for the influence of a subcutaneous fat layer. *Rev. Sci. Instrum.* **71**, 4571–4575 (2000).

Acknowledgement

The authors are grateful for funding support from the National Institutes of Health (NIH) R01-CA149274, R21-AR062356 and UL-1RR033173. The content is solely the responsibility of the authors and does not necessarily represent the official views of the NIH. We also thank Daniel Irwin for his help in reviewing the manuscript.

Author contributions

G.Y. conceived and supervised this project. T.L. wrote the initial manuscript; G.Y., T.L. and Y.L. revised the manuscript. Y.L. and G.Y. designed the noncontact probe. Y.L., L.H. and T.L. collected the data. T.L. and Y.L. analyzed the data. T.L. studied the curvature effect on measurements and performed MC simulations. C.H. prepared some figures. Y.S. provided technical assistance for data collection and analysis. M.S. participated in data interpretation. All authors reviewed and approved the manuscript.

Additional information

Competing financial interests: The authors declare no competing financial interests.

License: This work is licensed under a Creative Commons Attribution-NonCommercial-NoDerivs 3.0 Unported License. To view a copy of this license, visit <http://creativecommons.org/licenses/by-nc-nd/3.0/>

How to cite this article: Li, T. *et al.* Simultaneous measurement of deep tissue blood flow and oxygenation using noncontact diffuse correlation spectroscopy flow-oximeter. *Sci. Rep.* **3**, 1358; DOI:10.1038/srep01358 (2013).